Characterizing isolated attosecond pulses from hollow-core waveguides using multi-cycle driving pulses

I. Thomann[1], A. Bahabad[1], X. Liu[2], R. Trebino[2], M. M. Murnane[1] and H. C. Kapteyn[1]

[1] *JILA, University of Colorado and NIST, Boulder, Colorado 80309, USA*

[2] *School of Physics, Georgia Institute of Technology, Atlanta, Georgia 30332, USA*

Isabell.Thomann@Colorado.edu

Abstract: The generation of attosecond-duration light pulses using the high-order harmonic generation process is a rapidly evolving area of research. In this work, we combine experimental measurements with careful numerical analysis, to demonstrate that even relatively long-duration, 15 fs, carrier-envelope-phase (CEP) unstabilized near-infrared (NIR) pulses can generate isolated attosecond extreme-ultraviolet (EUV) pulses by the dynamically-changing phase matching conditions in a hollow-core waveguide geometry. The measurements are made using the laser-assisted photoelectric effect to cross-correlate the EUV pulse with the NIR pulse. A FROG CRAB analysis of the resulting traces (photoelectron signal versus photoelectron energy and EUV-NIR delay) is performed using a generalized projections (GP) algorithm, adapted for a wide-angle photoelectron detection geometry and non-CEP stabilized driving laser pulses. In addition, we performed direct FROG CRAB simulations under the same conditions. Such direct simulations allow more freedom to explore the effect of specific pulse parameters on FROG CRAB traces than is possible using the automated GP retrieval algorithm. Our analysis shows that an isolated pulse with duration of ≈ 200 attoseconds can result from CEP unstabilized, high intensity ≈ 15 fs multi-cycle driving pulses coupled into a hollow-core waveguide filled with low-pressure Argon gas. These are significantly longer driving pulses than used in other experimental implementations of isolated attosecond pulses.

OCIS codes: (120.0120) Instrumentation, measurement, and metrology.; (020.4180) Multiphoton processes; (300.6500) Spectroscopy, time-resolved; (340.0340) X-ray optics

References and links

1. I. Thomann, E. Gregonis, X. Liu, R. Trebino, A. Sandhu, M. Murnane, and H. Kapteyn, "Temporal characterization of attosecond waveforms in the sub-optical cycle regime," Phys. Rev. A, **78**, 011806(R) (2008).
2. K. Kulander, K. Schafer, and J. Krause, " Dynamics of short-pulse excitation, ion- ization, and harmonic conversion," in *Super-Intense Laser-Atom Physics*, B. Pi- raux, A. L'Huillier, and K. Rzazewski, Eds., vol. 316. Han-sur-Lesse, Belgium: Plenum, 1993, pp. 95-110.
3. M. Lewenstein, Ph. Balcou, M. Yu. Ivanov, A. L'Huillier, and P. B. Corkum, "Theory of high-harmonic generation by low-frequency laser fields," Phys. Rev. A **49,** 2117–2132 (1994).

#105342 - $15.00 USD Received 15 Dec 2008; revised 1 Mar 2009; accepted 5 Mar 2009; published 9 Mar 2009

4. P. B. Corkum, "Plasma Perspective on Strong-Field Multiphoton Ionization," Phys. Rev. Lett. **71,** 1994–1997 (1993).
5. J. Gagnon, E. Goulielmakis, and V. S. Yakovlev, "The accurate FROG characterization of attosecond pulses from streaking measurements," Appl. Phys. B **92,** 25–32 (2008).
6. Y. Mairesse, A. de Bohan, L. J. Frasinski, H. Merdji, L. C. Dinu, P. Monchicourt, P. Breger, M. Kovačev, R. Taïeb, B. Carré, H. G. Muller, P. Agostini, and P. Salières, "Attosecond Synchronization of High-Harmonic Soft X-Rays," Science **302,** 1540–1543 (2003).
7. R. López-Martens, K. Varjú, P. Johnsson, J. Mauritsson, Y. Mairesse, P. Salières, M. B. Gaarde, K. J. Schafer, A. Persson, S. Svanberg, C.-Göran Wahlström, and A. L'Huillier, "Amplitude and Phase Control of Attosecond Light Pulses," Phys. Rev. Lett. **94,** 033001 (2005).
8. G. Sansone, E. Benedetti, F. Calegari, C. Vozzi, L. Avaldi, R. Flammini, L. Poletto, P. Villoresi, C. Altucci, R. Velotta, S. Stagira, S. De Silvestri, and M. Nisoli, "Isolated Single-Cycle Attosecond Pulses," Science **314,** 442–446 (2006).
9. Gy. Farkas and Cs. Tòth, "Proposal for attosecond light pulse generation using laser induced multiple-harmonic conversion processes in rare gases," Phys. Lett. A **168** 447 - 450 (1992).
10. S. E. Hands, J. J Macklin, and T. W. Haensch, "Atomic scale temporal structure inherent to high-order harmonic generation," Opt. Commun. **100,** 487-490 (1993).
11. Z. Chang, "Single attosecond pulse and xuv supercontinuum in the high-order harmonic plateau," Phys. Rev. A **70,** 043802 (2004).
12. P. B. Corkum, N. H. Burnett, and M. Y. Ivanov, "Subfemtosecond pulses," Opt. Lett. **19,** 1870 - 1872 (1994).
13. E. Goulielmakis, M. Schultze, M. Hofstetter, V. S. Yakovlev, J. Gagnon, M. Uiberacker, A. L. Aquila, E. M. Gullikson, D. T. Attwood, R. Kienberger, F. Krausz, and U. Kleineberg, "Single-Cycle Nonlinear Optics," Science **320,** 1614–1617 (2008).
14. A. Rundquist, C. Durfee, Z. Chang, C. Herne, S. Backus, M. Murnane, and H. Kapteyn, "Phase-matched generation of coherent soft x-rays," Science **280,** 1412–1214 (1998).
15. M. Drescher, M. Hentschel, R. Kienberger, G. Tempea, C. Spielmann, G. A. Reider, P. B. Corkum, and F. Krausz, "X-ray Pulses Approaching the Attosecond Frontier," Science **291,** 1923–1927 (2001).
16. Y. Mairesse and F. Quéré,"Frequency-resolved optical gating for complete reconstruction of attosecond bursts," Phys. Rev. A **71,** 011401 (2005).
17. F. Quere, Y. Mairesse, and J. Itatani, "Temporal characterization of attosecond XUV fields," J. Mod. Opt. **52,** 339–360 (2005).
18. P. Kruit and F. H. Read, "Magnetic field paralleliser for 2π electron-spectrometer and electron-image magnifier," J. Phys. E - Scientific Instruments, **16,** 313–324 (1983).
19. M. Hentschel, R. Kienberger, Ch. Spielmann, G. A. Reider, N. Milosevic, T. Brabec, P. Corkum, U. Heinzmann, M. Drescher, and F. Krausz, "Attosecond metrology," Nature **414,** 509–513 (2001).
20. M. B. Gaarde and K. J. Schafer, "Generating single attosecond pulses via spatial filtering," Opt. Lett. **31,** 3188 - 3190 (2006).
21. H. Mashiko, S. Gilbertson, C. Li, E. Moon, and Z. Chang, "Optimizing the photon flux of double optical gated high-order harmonic spectra," Phys. Rev. A **77,** 063423 (2008).
22. H. Merdji, T. Auguste, W. Boutu, J.-Pascal Caumes, B. Carré, T. Pfeifer, A. Jullien, D. M. Neumark, and S. R. Leone, "Isolated attosecond pulses using a detuned second-harmonic field," Opt. Lett. **32,** 3134–1336 (2007).
23. T. Pfeifer, A. Jullien, M. J. Abel, P. M. Nagel, L. Gallmann, D. M. Neumark, and S. R. Leone, "Generating coherent broadband continuum soft-x-ray radiation by attosecond ionization gating," Opt. Express, **15,** 17120–17128 (2007).
24. W. Cao, P. Lu, P. Lan, X. Wang, and G. Yang, "Single-attosecond pulse generation with an intense multicycle driving pulse," Phys. Rev. A **74,** 063821 (2006).
25. I. P. Christov, H. C. Kapteyn, and M. M. Murnane, "Quasi-phase matching of high-harmonics and attosecond pulses in modulated waveguides" Opt. Express, **7,** 362–367 (2000).
26. U. Becker and D. Shirley, *VUV And Soft X-Ray Photoionization*, (Plenum Press New York 1996).
27. M. Nisoli, S. De Silvestri, O. Svelto, R. Szipöcs, K. Ferencz, Ch. Spielmann, S. Sartania, and F. Krausz, "Compression of high-energy laser pulses below 5 fs," Opt. Express, **22,** 522–524 (1997).
28. A. Suda, M. Hatayama, K. Nagasaka, and K. Midorikawa, "Generation of sub-10-fs, 5-mJ-optical pulses using a hollow fiber with a pressure gradient," Appl. Phys. Lett. **86,** 111116 (2005).
29. R. Trebino, *Frequency-Resolved Optical Gating: The Measurement of Ultrashort Laser Pulses*, (Kluwer Academic Publishers, Boston 2002).
30. R. Trebino, K. W. DeLong, D. N. Fittinghoff, J. N. Sweetser, M. A. Krumbgel, and D. J. Kane, "Measuring ultrashort laser pulses in the time-frequency domain using frequencyresolved optical gating," Rev. Sci. Instrum. **68,** 3277 (1997).
31. D. J. Kane, "Principal components generalized projections: a review," J. Opt. Soc. Am. B **25,** 120 (2008).
32. C. A. Haworth, L. E. Chipperfield, J. S. Robinson, P. L. Knight, J. P. Marangos, and J. W. G. Tisch, "Half-cycle cutoffs in harmonic spectra and robust carrier-envelope phase retrieval," Nature Phys. **3,** 52–57 (2007).
33. I. P. Christov, M. M. Murnane, and H. C. Kapteyn, "High-Harmonic Generation of Attosecond Pulses in the

#105342 - $15.00 USD Received 15 Dec 2008; revised 1 Mar 2009; accepted 5 Mar 2009; published 9 Mar 2009

"Single-Cycle" Regime," Phys. Rev. Lett. **78,** 1251–1254 (1997).
34. M. B. Gaarde, J. L. Tate, and K. J. Schafer, "Macroscopic aspects of attosecond pulse generation," J. Phys. B: At. Mol. Opt. Phys. **41,** 132001 (2008).
35. V. V. Strelkov, E. Mével, and E. Constant, "Generation of isolated attosecond pulses by spatial shaping of a femtosecond laser beam," New J. Phys. **10,** 083040 (2008).
36. C. Winterfeldt, C. Spielmann, and G. Gerber, "Colloquium: Optimal control of high-harmonic generation," Rev. Mod. Phys. **80,** 117–140 (2008).
37. T. Sekikawa, A. Kosuge, T. Kanai, and S. Watanabe, "Nonlinear optics in the extreme ultraviolet," Nature **432,** 605–608 (2004).
38. Y. Nabekawa, H. Hasegawa, E. J. Takahashi, and K. Midorikawa, "Production of Doubly Charged Helium Ions by Two-Photon Absorption of an Intense Sub-10-fs Soft X-Ray Pulse at 42 eV Photon Energy," Phys. Rev. Lett. **94,** 043001 (2005).
39. J. M. Schins, P. Breger, P. Agostini, R. C. Constantinescu, H. G. Muller, G. Grillon, A. Antonetti, and A. Mysyrowicz, "Observation of Laser-Assisted Auger Decay in Argon," Phys. Rev. Lett. **73,** 2180-2183 (1994).
40. T. E. Glover, R. W. Schoenlein, A. H Chin, and C. V. Shank, "Observation of laser assisted photoelectric effect and femtosecond high order harmonic radiation," Phys. Rev. Lett. **76,** 2468-2471 (1996).
41. P. M. Paul, E. S. Toma, P. Breger, G. Mullot, F. Augé, Ph. Balcou, H. G. Muller, and P. Agostini, "Observation of a Train of Attosecond Pulses from High Harmonic Generation," Science **292,** 1689–1692 (200).
42. J. Itatani, F. Quéré, G. L. Yudin, M.Yu. Ivanov, F. Krausz, and P. B. Corkum, "Attosecond Streak Camera," Phys. Rev. Lett. **88,** 173903 (2002).
43. E. Cormier, I. A. Walmsley, E. M. Kosik, A. S. Wyatt, L. Corner, and L. F. DiMauro, "Self-Referencing, Spectrally, or Spatially Encoded Spectral Interferometry for the Complete Characterization of Attosecond Electromagnetic Pulses," Phys. Rev. Lett. **94,** 033905 (2005).
44. K. Varjú, Y. Mairesse, B. Carré, M. B. Gaarde, P. Johnsson, S. Kazamias, R. López-Martens, J. Mauritsson, K. J. Schafer, PH. Balcou, A. L'huillier, and P. Salières, "Frequency chirp of harmonic and attosecond pulses," J. Mod. Opt. **52,** 379 – 394 (2005).
45. N. L. Wagner, E. A. Gibson, T. Popmintchev, I. P. Christov, M. M. Murnane, and H. C. Kapteyn, "Self-Compression of Ultrashort Pulses through Ionization-Induced Spatiotemporal Reshaping," Phys. Rev. Lett. **93,** 173902 (2004).
46. C. Altucci, V. Tosa, and R. Velotta, "Beyond the single-atom response in isolated attosecond-pulse generation," Phys. Rev. A **75,** 061401(R) (2007).
47. A. Baltuška, Th. Udem, M. Uiberacker, M. Hentschel, E. Goulielmakis, Ch. Gohle, R. Holzwarth, V. S. Yakovlev, A. Scrinzi, T. W. Hänsch, and F. Krausz, "Attosecond control of electronic processes by intense light fields," Nature **421,** 611 (2003).
48. M. Nisoli, G. Sansone, S. Stagira, and S. De Silvestri, C. Vozzi, M. Pascolini, L. Poletto, P. Villoresi, and G. Tondello, "Effects of Carrier-Envelope Phase Differences of Few-Optical-Cycle Light Pulses in Single-Shot High-Order-Harmonic Spectra," Phys. Rev. Lett. **91,** 213905 (2003).
49. G. Sansone, C. Vozzi, S. Stagira, and M. Nisoli, "Nonadiabatic quantum path analysis of high-order harmonic generation: Role of the carrier-envelope phase on short and long paths," Phys. Rev. A **70,** 013411 (2004).
50. S. Backus, R.Bartels, S. Thompson, R. Dollinger, H. C. Kapteyn, and M. M. Murnane, "High-efficiency, single-stage 7-kHz high-average-power ultrafast laser system," Opt. Lett. **26** 465 (2001).
51. Z. Chang, A. Rundquist, H. Wang, I. Christov, H. C. Kapteyn, and M. M. Murnane, "Temporal phase control of soft-x-ray harmonic emission," Phys. Rev. A **58,** 30(R) (1998).
52. E. A. Gibson, A. Paul, N. Wagner, R. Tobey, D. Gaudiosi, S. Backus, I. P. Christov, A. Aquila, E. M. Gullikson, D. T. Attwood, M. M. Murnane, and H. C. Kapteyn, "Coherent Soft X-ray Generation in the Water Window with QuasiPhase Matching," Science **302,** 95 (2003).
53. A. Sandhu, E. Gagnon, A. Paul, I. Thomann, A. Lytle, T. Keep, M. Murnane, H. Kapteyn, and I. Christov, "Generation of sub-optical-cycle, carrier-envelope-phase-insensitive, extreme-uv pulses via nonlinear stabilization in a waveguide," Phys. Rev. A **74,** 61803 (2006).
54. M. Geissler, G. Tempea, A. Scrinzi, M. Schnrer, F. Krausz, and T. Brabec, "Light Propagation in Field-Ionizing Media: Extreme Nonlinear Optics," Phys. Rev. Lett. **83,** 2930–2933 (1999).
55. C. Spielmann, C. Kan, N. Burnett, T. Brabec, M. Geissler, A. Scrinzi, M. Schnurer, and F. Krausz, "Near-keV coherent X-ray generation with sub-10-fs lasers," IEEE J. Sel. Top. Quantum Electron. **4,** 249–265 (1998).
56. P. Tzallas, E. Skantzakis, C. Kalpouzos, E. P. Benis, G. D. Tsakiris, and D. Charalambidis, "Generation of intense continuum extreme-ultraviolet radiation by many-cycle laser fields," Nature Physics **3,** 846–850 (2007).

1. Introduction

To date, sub-femtosecond light pulses have been generated only through the process of high-order harmonic generation (HHG). By the uncertainty principle, sub-femtosecond light pulses require a bandwidth larger than 10^{15}Hz, which is larger than the entire visible range of the spec-

#105342 - $15.00 USD Received 15 Dec 2008; revised 1 Mar 2009; accepted 5 Mar 2009; published 9 Mar 2009

trum. In HHG an intense ultrashort laser pulse is focused into a gas. The interaction between the atoms and laser field is so strong that a portion of the electron wave packet can escape the atom due to the lowering of the Coulomb potential by the laser electric field. The electron wave packet is then accelerated by the laser electric field, and forced back towards the atom as the sign of the field reverses. The returning electron wave packet can, with a certain probability, recombine with the ion and emit higher harmonics of the fundamental laser frequency [2, 3, 4]. As this process repeats in each half-cycle of the fundamental laser field, a comb of high harmonics is generated. Provided that the phases of the high harmonics are synchronized [6, 7] a train of attosecond ($= 10^{-18}$ s) duration pulses is generated. If the process of high harmonic generation can be limited to one half-cycle of the fundamental driving field, a continuous spectrum can be generated, and if the phase of the spectrum is appropriate, a single isolated attosecond pulse results. To-date, attosecond pulses have been generated only using very short-duration, 5-7 fs driving laser pulses. Using these very short-duration laser pulses [33, 13] the cycle-by-cycle electric field of the laser pulse changes significantly. Spectrally filtering to allow only the highest energy harmonic light to pass can then produce a single isolated attosecond pulse. Theoretically it has been shown that this approach requires 5 fs driving laser pulses [33]. A variation of this method adds a rapidly changing ellipticity to the driving laser pulse [8, 11, 12]. The efficiency of high harmonic generation is strong only for linearly polarized driving lasers, and falls strongly with ellipticity. In this scheme only a single half-cycle occurs which has linear polarization and therefore allows generation of high harmonics, whereas the elliptical polarization suppresses HHG in all other half-cycles. This ellipticity scheme was the first proposal to generate an isolated attosecond pulse [12], based on earlier suggestions of the attosecond pulse structure of high-harmonic generation [9, 10]. The original proposal suggested that driving pulses of 25 fs duration could be used to generate subfemtosecond pulses. The use of 25 fs driving pulses has proven to be over-optimistic (see however [56]); nevertheless, polarization modulation of a sub-10 fs driving pulse can broaden the region of the spectrum over which a continuum is generated, and thus helps to generate shorter-duration pulses.

Experimentally, all implementations of isolated attosecond pulses to-date have used carrier-envelope phase (CEP) stabilized driving pulses of 5 fs duration, with the exception of some earlier experimental results that showed evidence for the generation of single attosecond pulses of 650 ± 150 duration using 7.5 fs long driving laser pulses [19]. In detailed theoretical studies [20] the reason for generating a single isolated attosecond pulse using such long driving pulses was explained by "ionization driven spatio-temporal reshaping of the intense driving pulse as it propagates through a long, relatively dense medium leads to XUV radiation which, after spatial and spectral filtering in the far field, yields an isolated attosecond pulse". As CEP stabilized 5 fs pulses are difficult to work with, there is great interest in generating isolated single attosecond pulses using longer driving pulses e.g. by employing two-color laser driving fields, ionization gating, quasi-phase-matching, long-wavelength driving lasers, or spatial shaping of the driving pulse [21, 22, 23, 24, 25, 34, 35]. So far, these have been theoretical suggestions or spectral measurements, but with no temporal characterization of the emission generated in these longer-duration driving pulse regimes to date.

Characterizing the time structure of either attosecond pulse trains [7, 6] or isolated attosecond pulses [8, 13] is equally important and technically challenging to the generation process. There are several reasons for this. First, the generated radiation lies in the extreme ultraviolet (EUV) region and therefore is strongly absorbed in air or any material. As a consequence, experiments must be conducted inside a vacuum chamber. Second, as high harmonic generation is a highly nonlinear process, the EUV photon flux is typically low ($\approx 10^9$ photons/sec at 45 eV). For these reasons, instantaneous nonlinear effects that are commonly used in the visible region are difficult to access in the EUV regime. Therefore nearly [37, 38] all current

#105342 - $15.00 USD Received 15 Dec 2008; revised 1 Mar 2009; accepted 5 Mar 2009; published 9 Mar 2009

EUV pulse characterization techniques rely on two-color photoionization, in which an atom is simultaneously irradiated with EUV and near-infrared (NIR) laser fields, and the energy of the resultant electrons is monitored as a function of the time delay between the laser and EUV fields [39, 40]. Here the EUV radiation creates one or several electron wavepackets by single photon photoionization. These wavepackets are then modulated by the electric field of the NIR laser field, leading to sidebands or shifts in the resulting photoelectron spectra (see below). The resulting spectrogram as a function of delay τ and photoelectron energy ω encodes information about the temporal structure of the EUV pulse.

To extract the temporal structure of the attosecond fields, different methods have been proposed and some of them have been experimentally implemented [41, 42, 43]. For isolated attosecond pulses that are significantly shorter than the driving laser field, the "attosecond streak camera" technique has been used [42]. To reconstruct individual attosecond bursts of long attosecond pulse trains consisting of identical attosecond pulses, the "RABBITT" (Reconstruction of Attosecond Beating By Interference of Two-photon Transition) technique has been employed. As originally proposed, RABBITT used the sideband structure to extract the relative phase between harmonic orders, which relates directly to an averaged attosecond pulse structure. However it did not attempt to obtain information on the pulse envelope, e.g. through analysis of the detailed shape of the sidebands versus energy and delay. A more generally applicable method is the FROG-CRAB (Frequency Resolved Optical Gating for Complete Reconstruction of Attosecond Bursts) technique. This technique was theoretically proposed in [16, 17] and can in theory characterize attosecond fields of arbitrarily complex temporal structure. We chose this method to characterize recent experimental data [1] because they were exactly in the transition regime between an isolated single attosecond pulse and a train of attosecond pulses. That work demonstrated that, by using pulses of $\sim$ 13 fs duration in a phase-matched hollow-waveguide geometry, EUV pulses with envelope duration of 1.4 fs and individual pulse structure of $\sim$ 500 as could be generated. This corresponds to an attosecond pulse "train" that could contain 80% of its energy in a single burst, or consist of two equally strong bursts – the FROG CRAB measurement technique could only determine a pulse envelope and the structure of the individual attosecond bursts (but not their position) in this case of a non-CEP stabilized laser.

Despite all the efforts in characterizing experimental attosecond pulses, there are still unresolved issues in using attosecond pulse retrieval algorithms. Even the most current approaches fail to recover certain pulse parameters, e.g. do not yet give correctly the relative phase of adjacent EUV pulses [5]. Furthermore, so far no algorithm correctly includes the final photoelectron kinetic energy dependence in the FROG trace. This effect can be seen in [8] where the shifted photoelectron energies using the algorithm result in shifts that are too small at high photoelectron energies and too large at low photoelectron energies. The same effect can be seen in our results below when we retrieve the attosecond pulse using a GP (Generalized projections) algorithm [29, 30] that neglects the photoelectron kinetic energy dependence. The energy dependence is most important at low photoelectron energies and large ponderomotive shifts. Experiments in molecular dynamics using soft x-ray pulses often employ relatively low energy photons. Thus accuracy in characterizing all wavelength ranges is desirable.

This article has two major thrusts. The first is to describe the implementation of the GP FROG CRAB algorithm in the context of the conditions of this experiment- a wide-angle photoelectron detection geometry and non-CEP stabilized driving laser pulses. We also present direct simulations of FROG CRAB traces under these conditions. In these simulations we will focus on EUV fields in the intermediate regime between single isolated attosecond pulses and long attosecond pulse trains, since this is the parameter range where significant possible ambiguity exists in the pulse retrieval.

#105342 - $15.00 USD Received 15 Dec 2008; revised 1 Mar 2009; accepted 5 Mar 2009; published 9 Mar 2009

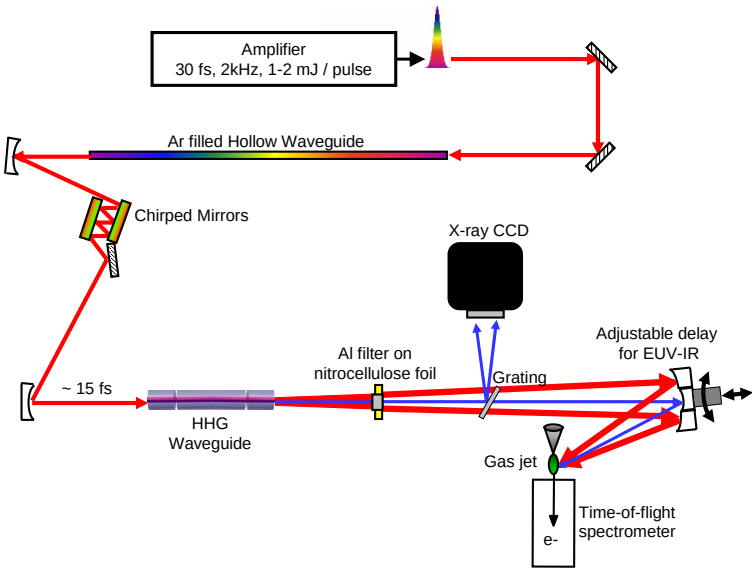

Fig. 1. Experimental setup for EUV pulse generation and temporal characterization via photoelectron energy resolved two-color cross-correlation using a NIR pulse.

Second, we present experimental energy-resolved interferometric EUV-NIR two-photon ionization cross correlation data where the EUV radiation was generated in an Argon filled hollow-core waveguide. In contrast to our previous work [1] where we studied EUV pulses generated from low intensity driving pulses and high Argon pressure inside the hollow-core waveguide, we show here that for high laser intensity and low Argon pressure inside the waveguide, a single isolated attosecond pulse can result from $\approx$ 15 fs CEP unstabilized driving pulses. These are significantly longer driving pulses than used in other experimental implementations of isolated attosecond pulses, and to our knowledge this is the first temporal characterization of single attosecond pulses generated from multi-cycle driving pulses. The radiation we describe is centered at energies around 42 eV.

The paper is organized as follows: In section 2 we describe the experimental setup. In section 3 we summarize the theory for atomic photoionization under the influence of a low-frequency driving laser field. Next we describe the GP algorithm (section 4) and its modifications for wide-angle photoelectron detection and CEP unstabilized driving pulses (section 5). In section 6 we describe our direct FROG CRAB simulations and compare them to results from the GP algorithm. In section 7 we give a qualitative picture for the generation of single isolated attosecond pulse under our experimental conditions. We end with an outlook on future extensions of this work.

2. Experimental setup and photoelectron detection geometry

Our experiment, shown in Fig. 1, starts with 30 fs, 2 mJ laser pulses from a cryogenically-cooled 2 kHz Ti:Sapphire laser amplifier [50]. We use a 1 m long, 400 μm diameter hollow waveguide filled with Argon gas to broaden the laser spectrum by self phase modulation (SPM fiber) [27, 28]. To prevent defocusing of the laser pulses at the entrance of the SPM fiber, we use a pressure gradient of 0 Torr at the input and $\sim$ 300 Torr at the output of the fiber. We then temporally compress the pulses using commercially-available negatively chirped mirrors (Layertec -40 fs^2 per mirror bounce). We obtain pulses of $\sim$ 15 fs duration centered at $\lambda \approx$

#105342 - $15.00 USD Received 15 Dec 2008; revised 1 Mar 2009; accepted 5 Mar 2009; published 9 Mar 2009

740 nm, and focus them into a 150 μm diameter, 3.5 cm long hollow-core waveguide (including two 0.5 cm long end sections for differential pumping) filled with Argon gas [14], in which the high harmonic radiation is generated. We estimate an intensity in the fiber of $\sim 5.7 \cdot 10^{14}$ W/cm^2, and the Argon pressure was ≈ 10 torr. We note that the coupling of the fundamental light into the fiber was well-optimized (80% coupling efficiency), resulting in very small power loss inside the fiber, and an excellent near-TEM_{00} output mode. This indicates near-perfect coupling to the fundamental EH_{11} fiber mode. The spectra of the fundamental radiation after the fiber showed only a small amount of blue-shift compared to the one before the fiber, indicating that only a small amount of temporal reshaping of the fundamental pulse took place in this low-pressure regime.

To temporally characterize the EUV pulse, we employ an interferometric, photoelectron energy resolved EUV - NIR cross correlation geometry [15]. The EUV and fundamental driving pulses are focused into a Neon gas jet, and a cross-correlation signal is obtained from the generated photoelectron spectra as the relative delay between the two pulses is varied. The delay line makes use of the different divergences of the fundamental and the EUV beam exiting the HHG fiber. The low divergence, central EUV beam passes through a small circular Al filter suspended in a Kapton filter. The annular fundamental beam, which passes around the Al filter, is reflected by an annular mirror, while the central EUV beam is reflected by a Mo/Si mirror that is mounted on a closed loop piezoelectric transducer (S-325 tip/tilt piezo and z-axis positioner, Physik Instrumente).

The photoelectrons ejected from Neon by the EUV beam are then detected using a magnetic bottle time-of-flight photoelectron spectrometer [18] and a multichannel plate (MCP) detector in a Chevron configuration. This spectrometer has a 2 π detection solid angle i.e. photoelectrons parallel and perpendicular to the laser polarization (which points towards the MCP) are detected. To characterize the EUV spectrum separately, we use a home-built EUV spectrometer consisting of a concave grating (ROC 1 m, 1200 gr/mm) and an x-ray CCD camera (100 x 1340 pixels, Roper Scientific), directly following the high harmonic generation hollow-core waveguide.

The resolution of the EUV spectrometer was determined in a separate measurement, in which very narrow harmonics were generated and then characterized with the EUV spectrometer. From the measured width of these harmonics, an upper limit on the EUV spectrometer resolution of 0.38 eV at 47 eV photon energy was determined. Simultaneously with this determination of an upper limit for the resolution of the EUV spectrometer, the photoelectron spectrum was measured and an upper limit for the resolution of the photoelectron spectrometer was determined to be 0.73 eV for electrons of a kinetic energy of ≈ 22 eV.

In Fig. 2 we show an experimental EUV spectrum using the x-ray spectrometer. The CCD spectrum shows a quasicontinuum centered around the 23^{rd} harmonic. We also show the corresponding unstreaked photoelectron spectrum, upshifted by the ionization potential of the gas. The difference in shape is due to the mirror reflectivity of Mo/Si EUV mirror used for focusing into the Neon detection gas jet (Mo/Si multilayer mirror centered at $\approx 47 eV$ with a FWHM $\approx 13 eV$). This mirror therefore provides a spectral filtering which suppresses the lower harmonics and results in a continuum centered around the 25^{th} harmonic. Despite some apparent differences in modulation depth between the two spectra, we have confirmed by fitting both spectra, that the average modulation depths in both spectra in the region from $37 eV - 47 eV$ that dominantly makes up the EUV pulse are actually the same, verifying that the photoelectron spectrometer resolution of $\approx 0.73 eV$ is sufficient to reproduce the spectral characteristics of the source. From the fitted modulation depth we qualitatively expect the EUV radiation to consist of one dominant attosecond pulse and a side burst of $\approx 10\%$ electric field strength (i.e. $\approx 1\%$ intensity). This expectation is confirmed by our quantitative analysis below.

#105342 - $15.00 USD Received 15 Dec 2008; revised 1 Mar 2009; accepted 5 Mar 2009; published 9 Mar 2009

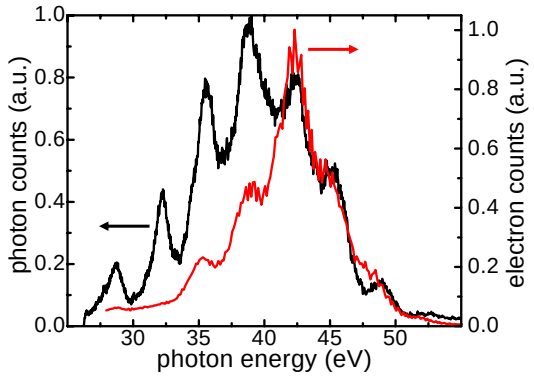

Fig. 2. EUV spectrum recorded with an x-ray spectrometer (black), and corresponding photoelectron spectrum upshifted by the ionization potential without the fundamental light present (red). The difference in spectral shape is due to EUV mirror reflectivity (which is low at the lower photon energies).

3. Theoretical background: EUV photoionization in the presence of a NIR driving laser field

FROG CRAB is inspired by the temporal characterization technique FROG, which is well established for the characterization of short laser pulses in the mid-IR to UV region of the spectrum [29, 30]. Ultrashort laser pulses in the visible/ NIR can be straightforwardly measured by making use of nonlinear-optical materials for this spectral region that operate at easily achievable intensities and have an instantaneous response. A commonly used nonlinear process is second-harmonic-generation (SHG). There a beamsplitter is used to split the pulse into two pulses i.e. one creates a replica of the pulse. This replica can then be delayed w.r.t the pulse in the other arm using a delay stage. The replica thereby serves as a temporal gate, sampling the spectrum of the pulse at varying delay steps. A two-dimensional trace of spectra versus delay steps is the result. This so-called spectrogram $S(\omega,\tau)$ can be mathematically written as

$$S(\omega,\tau)=\left|\int_{-\infty}^{+\infty}E(t)g(t-\tau)\exp\left(-i\omega t\right)dt\right|^2 \tag{1}$$

where $E(t)$ is the electric field and $g(t-\tau)$ is the gate function which is simply $E(t-\tau)$ in the case of SHG FROG. From the measured spectrogram the complete electric field can be determined using iterative Fourier-transform algorithms.

As first discussed in [16, 17], FROG CRAB extends FROG to the EUV and for attosecond pulses. For completeness we include here the main results of Quéré et. al. [16, 17] where they describe photoionization of atoms by EUV pulses in the presence of low-frequency driving pulses. The derivation assumes the strong field approximation (i.e. neglects the effect of the ionic potential on the motion of the electron after ionization) and the single active electron approximation. First, EUV radiation creates one or several electron wavepackets by single photon photoionization, which are then modulated by the electric field of the NIR laser leading to sidebands or shifts in the generated electron wavepackets. Mathematically the transition amplitude of the electron wavepacket $a_{\mathbf{v}}(\tau)$ at a delay time τ from the ground state to the final continuum state $|\mathbf{v}>$ with final electron velocity $\mathbf{v}$ is given by

$$a_{\mathbf{v}}(\tau)=-i\int_{-\infty}^{+\infty}\mathbf{d}_{\mathbf{p}(t)}\cdot\mathbf{E}_{xray}(t-\tau)\exp\left(i\left[I_p t-\int_t^{+\infty}\frac{p^2(t')}{2}dt'\right]\right)dt \tag{2}$$

#105342 - $15.00 USD Received 15 Dec 2008; revised 1 Mar 2009; accepted 5 Mar 2009; published 9 Mar 2009

Here $\mathbf{d}_{\mathbf{p}(t)}$ is the dipole transition matrix element from the ground state to the continuum state $|\mathbf{p}>$, $\mathbf{p}(t) = \mathbf{v} + \mathbf{A}(t)$ is the instantaneous momentum of the free electron in the laser field. Here $\mathbf{A}(t)$ is the vector potential such that $\mathbf{E}_{LASER}(t) = -\frac{\partial \mathbf{A}}{\partial t}$, and $\mathbf{E}_{xray}(t-\tau)$ is the electric field of the EUV pulse and I_p is the ionization potential of the atom. The term in the exponential is the acquired phase in the ground state until ionization at time t, and the Volkov phase i.e. the integral of the instantaneous energy of a free electron in the laser field.

Because there is no general description of the dipole transition matrix element $\mathbf{d}_{\mathbf{p}(t)}$, it is expedient to assume that it takes a constant value independent of energy. However this could lead to a photoelectron amplitude versus energy being different from the EUV pulse amplitude. Therefore the ionization cross section versus energy should ideally be taken into account in the fit process, or the EUV spectrum should be independently measured by a x-ray spectrometer. The EUV spectrum and photoelectron spectrum might also differ in phase if there is a phase dependence of the transition dipole matrix element as a function of energy (e.g. resonances in the continuum).

We can rewrite the amplitude of the electron wavepacket

$$a_{\mathbf{v}}(\tau) = -i \int_{-\infty}^{+\infty} \exp\left(i\Phi(t)\right) \mathbf{d}_{\mathbf{p}(t)} \cdot \mathbf{E}_{xray}(t-\tau) \exp\left(i(I_p + W)t\right) dt \tag{3}$$

where

$$\Phi(t) = -\int_{t}^{+\infty} \left(\mathbf{v} \cdot \mathbf{A}(t') + \frac{\mathbf{A}^2(t')}{2} \right) dt' \tag{4}$$

Since we are measuring photoelectron probabilities, the modulus square of the amplitude of the electron wavepacket, $|a_{\mathbf{v}}(\tau)|^2$ needs to be compared to the spectrogram $S(\omega, \tau)$. The one-by-one comparison shows that the gate function $g(t-\tau)$ of $S(\omega, \tau)$ corresponds to the $\exp\left(i\Phi(t)\right)$ term in $|a_{\mathbf{v}}(\tau)|^2$:

$$g(t) = \exp\left(i\Phi(t)\right) \tag{5}$$

This term corresponds to a phase modulation of the electron wavepacket induced by the NIR dressing laser, which serves as a temporal phase gate for measuring the duration of the EUV pulse.

Finally we express the phase with experimental observables as a sum of three contributions:

$$\Phi(t) = \Phi_1(t) + \Phi_2(t) + \Phi_3(t) \tag{6}$$

$$\Phi_1(t) = -\int_{t}^{+\infty} U_p(t) dt \tag{7}$$

$$\Phi_2(t) = \frac{\sqrt{8WU_p(t)}}{\omega_L} \cos(\theta) cos(\omega_L t - \phi_{CE}) \tag{8}$$

$$\Phi_3(t) = -\frac{U_p(t)}{2\omega_L} \sin(2\omega_L t - 2\phi_{CE}) \tag{9}$$

where

$$U_p(t) = \frac{E^2}{4\omega_L^2} \exp(-4\ln 2 (t/\tau)^2) \tag{10}$$

is the ponderomotive potential, W is the final photoelectron kinetic energy, ω_L is the laser angular frequency, and ϕ_{CE} is the fundamental carrier envelope phase, θ is the angle between the laser polarization direction and the final photoelectron velocity.

#105342 - $15.00 USD Received 15 Dec 2008; revised 1 Mar 2009; accepted 5 Mar 2009; published 9 Mar 2009

4. Generalized projections algorithm for FROGCRAB

We start by using the generalized projection (GP) algorithm to retrieve the EUV electric field. This iterative Fourier-transform algorithm converges to a solution by iteratively optimizing between two constraints - one in the frequency and one in the time domain. In the frequency domain, the calculated FROG trace amplitude is replaced by the square root of the experimental trace $S(\omega,\tau)$, and in the time domain a new guess for the electric field is obtained by minimizing the error between a newly created signal field $E_{sig}(t,\tau)$ and the signal field obtained in the last iteration $E'_{sig}(t,\tau)$.

A schematic of the procedure is shown in Fig. 3. First, a random $E_{xray}(t)$ is generated. Sec-

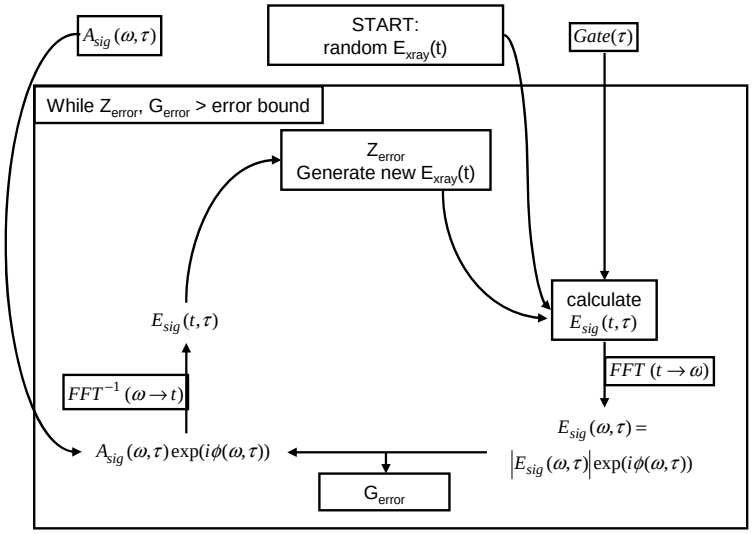

Fig. 3. Basic schematic of GP algorithm.

ond, a signal field

$$\mathbf{E}_{sig}(t,\tau) = E_{xray}(t-\tau)\exp(i\Phi(t)) \tag{11}$$

is generated. We note that the gate function is a user-input to the algorithm - it is not retrieved by the algorithm. It is important to note here that all current implementations of the GP algorithm, including ours, replace the final photoelectron kinetic energy W in Eq. (8) by W_0, the photoelectron center energy - we will discuss consequences of this approximation below. Third, Fourier-transforming into the frequency domain yields $E_{sig}(\omega,\tau)$. Fourth, the amplitude of $E_{sig}(\omega,\tau)$ is replaced by the amplitude $A_{sig}(\omega,\tau)$ of the experimental Frog trace data $S(\omega,\tau)$. Fifth, we perform the inverse Fourier-transform back into time domain $E'_{sig}(t,\tau)$. Sixth, we improve our guess for $E_{xray}(t)$ by minimizing the error between a newly created signal field and the signal field obtained in the last iteration. Seventh, the newly generated $E_{xray}(t)$ is used as input for a new signal field, which brings us back to the second step of the loop. The retrieval algorithm is run until the errors in the frequency domain

$$G_{err} = \sqrt{\frac{1}{N^2}\sum_{i,j=1}^{N}\left|A^2_{sig}(\omega_i,\tau_j) - \mu\,|E_{sig}(\omega_i,\tau_j)|^2\right|^2} \tag{12}$$

and in the time domain

#105342 - $15.00 USD Received 15 Dec 2008; revised 1 Mar 2009; accepted 5 Mar 2009; published 9 Mar 2009

$$Z_{err} = \sum_{i,j=1}^{N} \left| E_{sig}(t_i, \tau_j) - E'_{sig}(t_i, \tau_j) \right|^2 \tag{13}$$

are lower than a specified limiting value. Here μ is a real normalization constant that minimizes G_{err} and NxN is the array size.

5. Modifications to GP algorithm

Our experimental setup described above uses a magnetic bottle time-of-flight spectrometer that collects a large range of final electron momenta corresponding to angles from 0 to 90 degrees. In previous implementations of FROG CRAB, a narrow-angle photoelectron detection geometry was employed in order to obtain a well-defined phase-gate [8, 13]. In this work we show that EUV pulse reconstruction is possible also when a wide-angle detection geometry is employed, by a suitable averaging over FROG CRAB traces with different detection angles. Furthermore in our experiment, the CEP of the pulses is not stabilized. Both these features require modifications to the GP algorithm. The reason lies in the dependence of the gate function (5) on the angle θ and on the carrier-envelope phase of the NIR pulse, as seen in Eq. (3) to (10) in section 3. So, in essence one must run the algorithm with different gate functions in parallel, and do appropriate averaging when comparing with experimental data. In addition, the resolution of the photoelectron spectrometer should be included to take into account any broadening of the spectrum which leads to retrieved pulse durations systematically shorter than the actual pulse duration. In this experimental work, we use a very conservative value for this resolution, and thus obtain a result that is a realistic upper limit of pulse duration. The lower limit can be determined by the transform limit of the EUV spectrum.

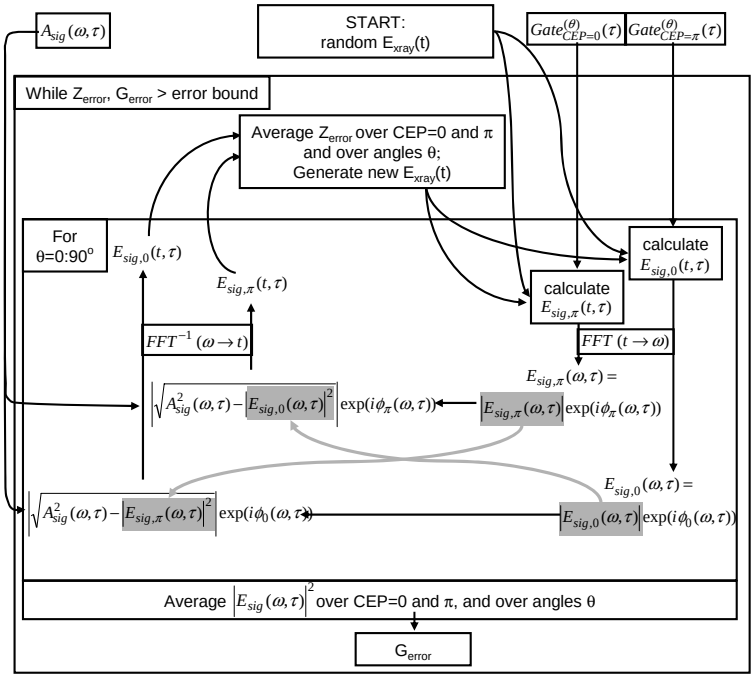

Fig. 4. Schematic of GP algorithm adapted to wide-angle photoelectron detection geometry and non-CEP stabilized driving laser pulses.

#105342 - $15.00 USD Received 15 Dec 2008; revised 1 Mar 2009; accepted 5 Mar 2009; published 9 Mar 2009

Figure 4 shows how the GP algorithm is modified to take into account the $2-\pi$ detection geometry and non-CEP stabilized IR pulses.

First, to take into account the fact that we make no attempt to CEP-stabilize our driving laser pulses, we take into account two gate functions - one with the absolute phase set to zero degree and one with the absolute phase set to 180 degrees. These CEP values correspond to "cosine" and "minus cosine" IR pulses which lead to identical conditions for HHG generation in a noble gas. Our results below show that the experimental data are quite well described by this procedure. The reason why only these two values of CEP are required to achieve good agreement is that the NIR beam (which is the same beam that generated the EUV radiation) is temporally synchronized with the EUV radiation due to the EUV generation process itself. However if multiple EUV bursts are present, their relative strengths (amplitudes, not their timing) could change with CEP. In our case, if for certain CEP values multiple bursts were generated, we would observe this as a modulation of the photoelectron spectrum, as shown in the simulations presented in Fig. 9. Experimentally however, we observe only a very small amount of modulation (see Fig. 2 and Fig. 9), meaning either that only in a small fraction of laser shots multiple EUV bursts are generated, or that in every shot only very small side bursts are generated along with the main burst. The synchronization is also well-demonstrated by the fact that we clearly see interferometric modulation of the photoelectron energy data versus delay (see Fig. 6 (a)). This is also not any more of an approximation than that used in any other attosecond pulse measurement. All measurements, whether they be for isolated pulses or pulse trains, show this interferometric synchronization [6, 19]. Furthermore, at the level of the instantaneous electric field of the driving laser, CEP fluctuations look identical to intensity fluctuations in the laser pulse, and recent theoretical calculations have corroborated the insensitivity of the pulse generation process to intensity variations [8]. Thus, our presumption that the attosecond pulses in the train are well-synchronized with the fundamental electric field, with the exception that the direction of the field oscillations may flip randomly, is well justified. The remaining question, which we address below, is whether the averaging over 2 CEP phases creates significant deconvolution ambiguities compared with a CEP-stabilized case.

We therefore apply the algorithm simultaneously to two signal fields - one with the CEP set to 0 degrees and one with CEP 180 degrees. Instead of replacing the amplitude of $\mathbf{E}_{sig}(\omega,\tau)$ by the amplitude of the experimental FROG CRAB trace $A_{sig}(\omega,\tau)$, we replace the amplitude of the signal field with CEP 0 radians $|E_{sig,0}(\omega,\tau)|$ with an expression containing the amplitude of the experimental FROG CRAB trace $A_{sig}(\omega,\tau)$ and the amplitude of the signal field with CEP π radians $\left|\sqrt{A_{sig}(\omega,\tau)^2-|E_{sig,\pi}(\omega,\tau)|^2}\right|$. An analogous replacement is made for $|E_{sig,\pi}(\omega,\tau)|$. This is the essential step of driving both signal fields to converge to a combined signal field describing the experimental FROG CRAB data. To obtain the G_{err} we calculate the rms error between the combined signal field

$$|E_{sig}(\omega,\tau)|^2=\frac{1}{2}\left(|E_{sig,0}(\omega,\tau)|^2+|E_{sig,\pi}(\omega,\tau)|^2\right) \tag{14}$$

and the experimental FROG CRAB trace. In the next step we Fourier-transform both signal fields back into time domain, yielding $E_{sig,0}(t,\tau)$ and $E_{sig,\pi}(t,\tau)$. Two new guesses for the EUV field $\mathbf{E}_{xray}(t)$ are calculated. The average of the two EUV fields is taken and used to construct two new signal fields $E'_{sig,0}(t,\tau)$ and $E'_{sig,\pi}(t,\tau)$. The Z_{err} is calculated for both CEP 0 and π according to Eq. (13), and is then averaged.

Next we discuss how to adapt the algorithm to include the dependence of the gate on the angle between the laser polarization and the final photoelectron velocity. To this end we implement a for-loop in which for each angle, both signal fields $E_{sig,0}(\omega,\tau)$ and $E_{sig,\pi}(\omega,\tau)$ are calculated. In the "replace magnitude" step (see Fig. 4) one should now in principle replace for every θ_0

#105342 - $15.00 USD Received 15 Dec 2008; revised 1 Mar 2009; accepted 5 Mar 2009; published 9 Mar 2009

the magnitude of $|E_{sig,0}(\omega,\tau,\theta_0)|^2$ with the expression $|A_{sig}(\omega,\tau)|^2 - \sum_{\theta\neq\theta_0}|E_{sig,0}(\omega,\tau,\theta)|^2 \cdot prob(\theta) - \sum_\theta |E_{sig,\pi}(\omega,\tau,\theta)|^2 \cdot prob(\theta)$. However to keep computations simple, we implemented a simplified replacement $|E_{sig,0}(\omega,\tau,\theta_0)| \rightarrow |\sqrt{A_{sig}(\omega,\tau)^2 - |E_{sig,\pi}(\omega,\tau,\theta_0)|^2}|$. This somewhat simplified approach is justified by the rapid and stable convergence of the algorithm to a solution for the EUV field that is essentially the same as the one found from the independent method of direct simulations of the FROG CRAB trace.

The G_{err} is then calculated with the average signal field calculated as a sum over different angles

$$E_{sig,CALC}(\omega,\tau) = \sqrt{\sum_\theta \left(|E^\theta_{sig,0}(\omega,\tau)|^2 \cdot prob(\theta) + |E^\theta_{sig,\pi}(\omega,\tau)|^2 \cdot prob(\theta) \right)} \tag{15}$$

where

$$prob(\theta) = \sin(\theta)\cdot\sigma(\theta) / \sum_\theta \sin(\theta)\cdot\sigma(\theta) \tag{16}$$

is the probability containing the geometrical weight factor $\sin(\theta)$ for the photoelectron distribution as well as the differential partial cross section $\sigma(\theta)$ for the detection gas used [26]. The ionization cross section used is $\sigma(\theta) \sim 1 + \beta \cdot P_2(cos(\theta))$ where P_2 is the second order Legendre polynomial, with $\beta = 0.8$ for Neon at $42\,eV$ photon energy. We also generate a for-loop to calculate the Z_{err} for all angles and we average the Z_{err} by calculating

$$Z_{err} = \sum_\theta Z_{err}(\theta) \cdot prob(\theta) \tag{17}$$

The $E_{xray}(t)$ is also averaged

$$E_{xray}(t)_{ave} = \sum_\theta E_{xray}(t,\theta) \cdot prob(\theta) \tag{18}$$

The resolution of the spectrometer can be included as follows. After calculating the new signal fields $E_{sig,0}(t,\tau)$ and $E_{sig,\pi}(t,\tau)$ in time, they are Fourier-transformed into the frequency domain and convolved with the square root of the resolution function of the photoelectron spectrometer. When in the next step the magnitude of $|E_{sig}(\omega,\tau)|$ is replaced (see Fig. 4), the information about the convolution is preserved in the phase of $E_{sig}(\omega,\tau)$, which remains unchanged. Empirically we found two further methods for improving the convergence of the algorithm: for every iteration, we vary the delay of the experimental trace by a fixed number of single delay steps to minimize the G_{err}. We also change the sign of the spectral phase of E_{xray} every ≈ 100 iterations. Only the center 90% of the delay range of the calculated FROG CRAB trace is used to calculate the G_{err}. This is done to avoid numerical artifacts that occur at the calculated edges.

To accurately retrieve an EUV pulse, we obtained high temporal resolution data for 2.5 laser cycles near to zero delay, with delay steps of 100 attoseconds. For such a "partial" FROG CRAB trace to converge, however, it is necessary to terminate the trace with a range of "unstreaked" spectra. Therefore we used a photoelectron spectrum generated by the EUV radiation alone and attached it at the edges (around ± 15 fs delay) of the experimental FROG CRAB trace as seen in Fig. 5. The convergence errors are calculated only for regions where data actually exist.

Figure 6 shows the experimental photoelectron energy resolved two-color cross-correlation and the FROG CRAB trace retrieved using the GP algorithm, as well as the EUV reconstructed electric field and intensity. Here, the G_{error} was 1.7%. The retrieved single isolated attosecond pulse has a FWHM pulse duration of 210 attoseconds with negligible ($\sim 5\%$ electric field amplitude) sidebursts, and a second-order dispersion of 0.009 fs^2. The agreement in the central

#105342 - $15.00 USD Received 15 Dec 2008; revised 1 Mar 2009; accepted 5 Mar 2009; published 9 Mar 2009

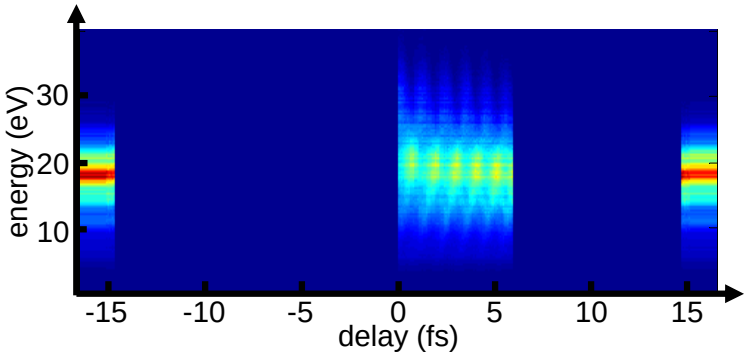

Fig. 5. Retrieval of a partial FROG CRAB trace. Experimentally, a small range ($0-6$ fs) of delay steps were taken with high temporal resolution. In order to retrieve the EUV pulse, the data are embedded into a larger array with zeros, with "unstreaked" spectra (recorded without the fundamental light present) attached at large delays.

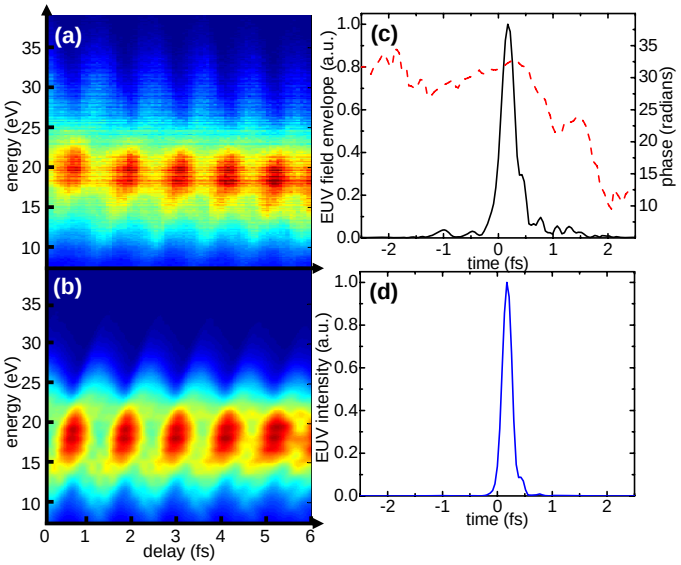

Fig. 6. (a) Zoom-in on the experimental photoelectron energy resolved two-color cross-correlation shown in Fig. 5. (b) FROG CRAB trace retrieved using the GP algorithm. The gate function was thoroughly optimized by running the algorithm multiple times to find the gate parameters which overall minimize the G error. The optimized gate uses a 15 fs fundamental Gaussian pulse with $U_p = 0.3\,eV$ and a linear chirp of $\Gamma_2 = 0.0178\,fs^2$. (c) Reconstructed EUV electric field envelope and temporal phase. (d) Reconstructed EUV intensity yielding a FWHM pulse duration of 210 attoseconds.

#105342 - $15.00 USD Received 15 Dec 2008; revised 1 Mar 2009; accepted 5 Mar 2009; published 9 Mar 2009

energy range is good, while at high energies, the ponderomotive shifts are not correctly recovered using the algorithm. This is due to the approximation of the W-dependence in Eq. (8) by W_0, as we will show below.

6. Direct simulations of FROG CRAB traces

In this section we employ directly simulated FROG CRAB traces. We first show that such direct simulations can reproduce the experimental two-color cross-correlation spectrogram shown in Fig. 6(a). Such direct simulations allow more freedom to explore the effect of specific pulse parameters on FROG traces, or to address specific concerns regarding the retrieved pulse, than is possible using the automated GP retrieval algorithm. We then turn to a more general discussion, showing that in almost all situations, the EUV electric field can be retrieved without carrier-envelope phase stabilization, with one important exception that we point out explicitly. Finally, we show that in direct simulations, which in contrast to the GP algorithm do not require the approximation $W->W_0$ in Eq. (8), the large ponderomotive upshifts seen in the experimental trace are reproduced correctly.

To simulate FROGCRAB traces, we employed the theory described in section 3, and adapted it to our experimental situation, again by appropriately weighting FROG CRAB traces obtained for different angles θ, and for CEP $= 0$ and CEP $= \pi$. All simulated traces were convolved with the experimentally measured photoelectron spectrometer resolution function, a Gaussian of 0.73 eV FWHM.

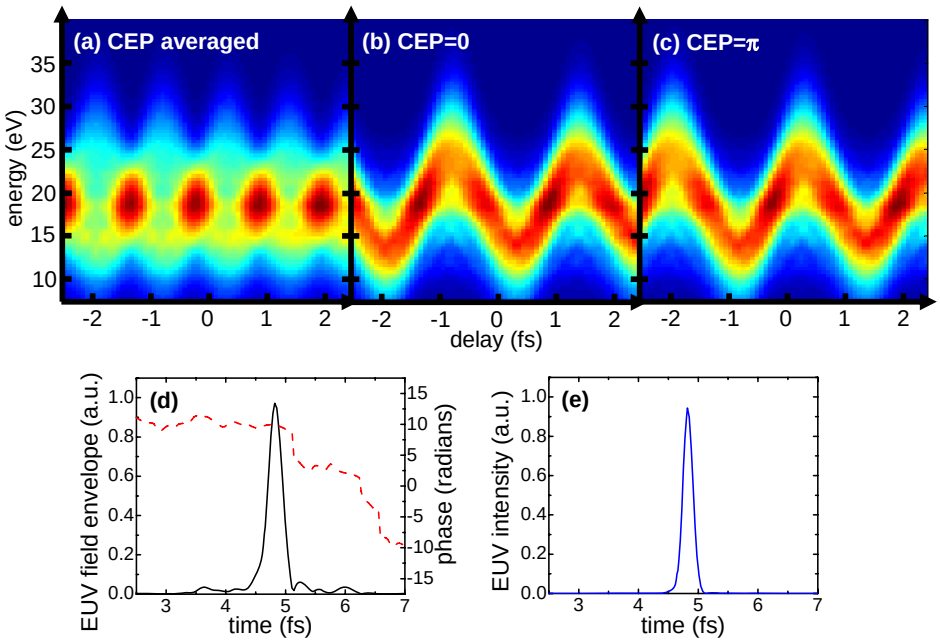

Fig. 7. Simulations for (a) averaged CEP, (b) CEP $= 0$, (c) CEP $= \pi$, (d) retrieved EUV field envelope and phase, (e) intensity of 200 attoseconds FWHM pulse duration

In Fig. 7 we show the results of the direct simulations yielding the best fit to the experimental data shown in Fig. 6(a). In addition to the final averaged trace (Fig. 7(a)), we also show the individual traces for CEP $= 0$ and CEP $= \pi$ (Fig. 7(b) and (c)). The retrieved single isolated attosecond pulse has a FWHM pulse duration of 200 ± 25 attoseconds, in good agreement with the result from the algorithm, and a second-order dispersion of $0.005\ fs^2$. The error in the pulse

#105342 - $15.00 USD Received 15 Dec 2008; revised 1 Mar 2009; accepted 5 Mar 2009; published 9 Mar 2009

duration was determined by an observation of a clearly visible discrepancy between measured and simulated FROG traces. The Fourier limited duration was 185*as*. We again point out that in these direct simulations we do *not* make the approximation $W->W_0$ in Eq. (8), yielding improved agreement in the strongly streaked regions compared to the GP algorithm (Fig. 6).

To generate the FROG CRAB trace above, first the gate function (i.e. the fundamental field) was obtained by optimizing agreement between simulation and full trace experimental data taken at larger delay steps of 300 attoseconds. These data are shown in Fig. 8. The retrieved fundamental pulse has a FWHM pulse duration of $15\,fs$, $U_p = 0.54eV$ and a linear chirp of $\Gamma_2 = 0.0185\,fs^{-2}$.

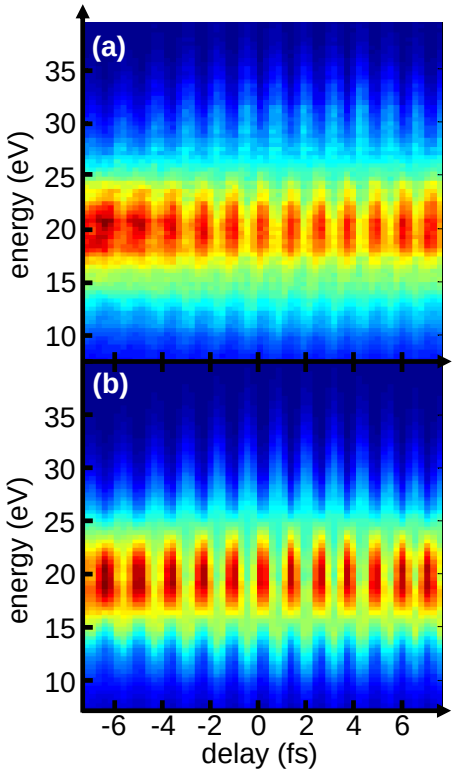

Fig. 8. (a) Experimental data of complete FROG CRAB trace (b) Simulations of experimental data shown in (a), used to extract NIR fundamental pulse parameters

Secondly, the simulated FROG CRAB traces were optimized with respect to the experimental FROG CRAB traces through a progressive fitting procedure by minimizing the root-mean-square (RMS) deviation between the simulated and experimental FROG CRAB traces. To this end, we include spectral phase terms describing the attochirp [44] resulting in a chirped x-ray field in time which is used as input in the simulations.

We used direct simulations to explore the question whether the measured FROG CRAB trace might be explained by an attosecond pulse train, as opposed to a single burst. In the case of an unchirped pulse train, already the CCD spectrum would reveal a comb of well resolved harmonics, contrary to what we observe in Fig. 2. Therefore we explored the possibility of a pulse train with a significant femtochirp [44, 51]. In this case subsequent portions of the train would generate energy-shifted harmonic combs, such that the time-integrated measured spectrum appears as a continuum. We explored a wide range of values for Γ_2, and find that

#105342 - $15.00 USD Received 15 Dec 2008; revised 1 Mar 2009; accepted 5 Mar 2009; published 9 Mar 2009

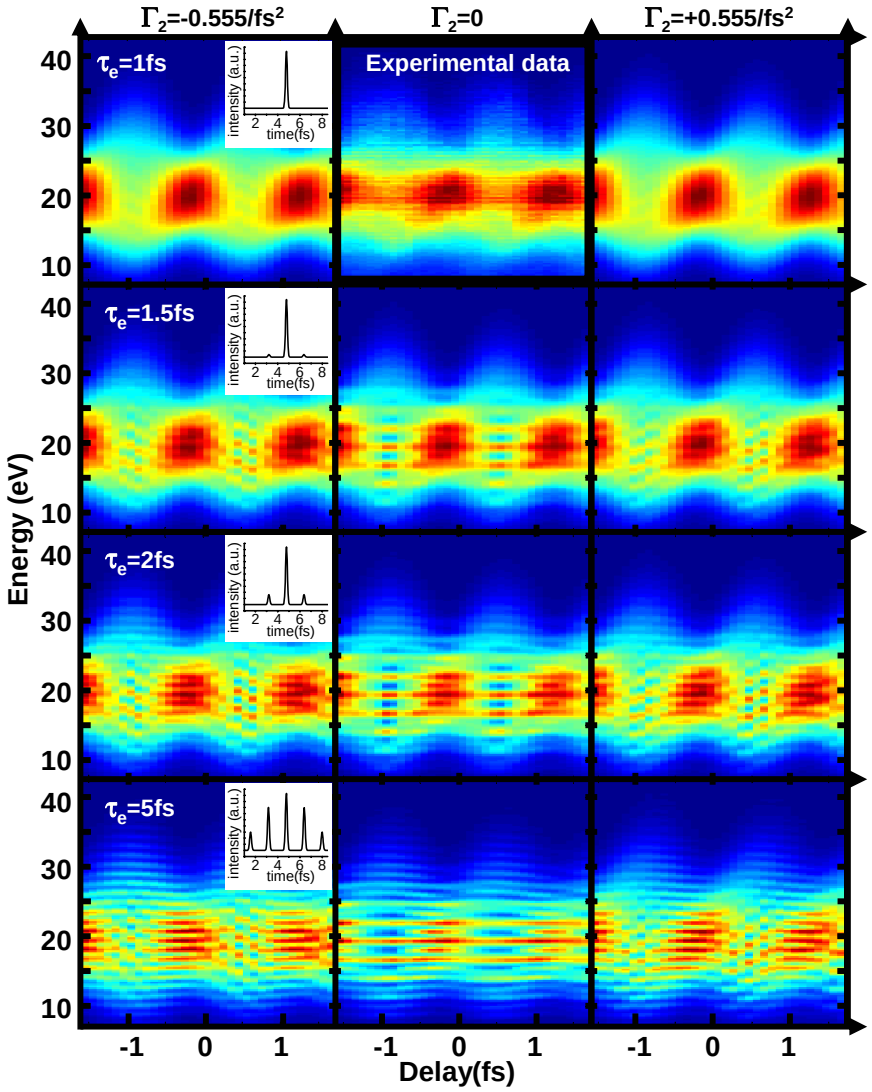

Fig. 9. Simulations of chirped attosecond pulse trains. Top row center: experimental data for comparison. Γ_2: femtochirp parameter in $1/fs^2$. τ_e: envelope of the simulated EUV pulse trains (see insets). First row: $\tau_e = 1$ fs corresponds to an isolated attosecond pulse with two, 10^{-3} intensity side bursts. $\tau_e = 1.5$ fs: two, 5% intensity side bursts. All simulated traces with $\tau_e > 1.5$ fs show significantly more spectral modulation than the experimental data. Simulated traces have been convoluted with the experimental photoelectron spectrometer resolution function.

#105342 - $15.00 USD Received 15 Dec 2008; revised 1 Mar 2009; accepted 5 Mar 2009; published 9 Mar 2009

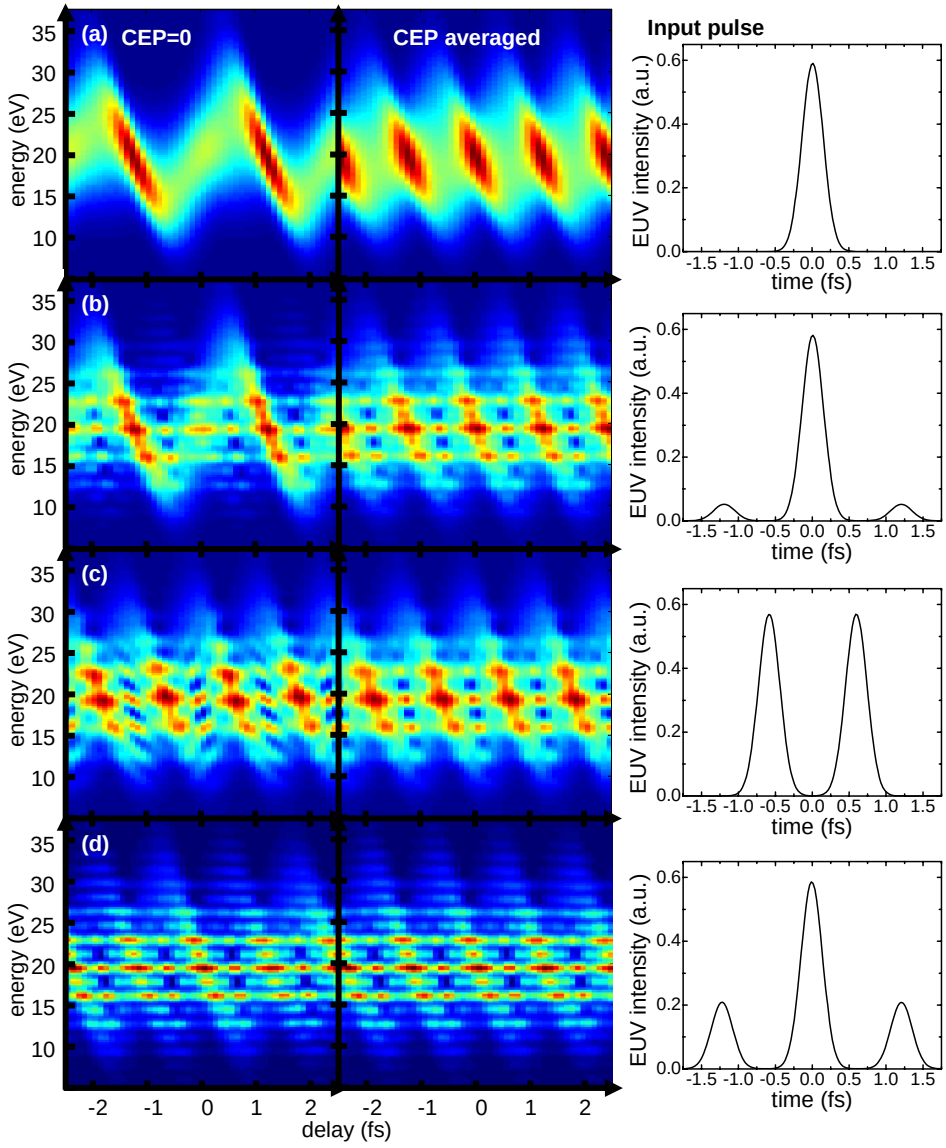

Fig. 10. Simulations of FROG CRAB traces for different number of EUV bursts. Left column: CEP stabilized traces; middle column: CEP unstabilized traces obtained by averaging over CEP 0 and π; right column: EUV intensity of input pulses

#105342 - $15.00 USD Received 15 Dec 2008; revised 1 Mar 2009; accepted 5 Mar 2009; published 9 Mar 2009

such FROG CRAB traces are always significantly modulated. Representative simulated data are shown in Fig. 9. From the amount of modulation in the calculated FROG CRAB traces, in comparison to experiment, we can set an upper limit on the energy contained in possible side bursts, of about 5%. Although it is impossible to test for all possible chirp patterns, our results strongly suggest that our experimental data are incompatible with a strongly chirped attosecond pulse train.

A last point of concern is the following: A number of measurements so-far have shown that the harmonic peaks in a spectrum can under certain conditions shift with the CEP value [47, 48]. However these observations were all made with very short driving pulses of ~ 6 fs duration. We have calculated the phase that the electron acquires while in the continuum (harmonic phase) using the classical electron trajectory for the short quantum path. It is the difference in this phase between the two dominant half-cycles contributing to radiation (see Fig. 12 below) that determines the spectral position of harmonic peaks. We calculate this harmonic phase difference for different values of the CEP, and find that for our harmonics in the plateau region the corresponding shifts of harmonic peaks in frequency are negligible (~ 0.2 eV) [48]. This is in agreement with earlier calculations using the saddle-point approximation that find strong effects of CEP on high harmonic generation in the high-plateau and cutoff region only when very short driving pulses are used [49], whereas the amount of CEP-dependent spectral shift of the harmonic peaks decreases upon increasing the driving pulse duration.

We now turn to a more general discussion of the possible ambiguities in CEP unstabilized vs. stabilized FROG traces. The left column of Fig. 10 shows simulated FROG CRAB traces for a single gate of CEP=0 radians, as would be measured in an experiment with CEP stabilized pulses, while the right column shows FROG traces averaged over two gates (CEP $= 0$ and CEP $= \pi$ radians). The figure shows that both for isolated attosecond bursts (Fig. 10(a)) as well as for attosecond pulse trains containing more than 2-3 bursts (Fig. 10(d)), the CEP does not need to be stabilized for reconstruction of the temporal structure of the EUV field. Only when working in the regime intermediate between a single isolated attosecond pulse with small $\approx 10\%$ intensity pre- and post pulses, (Fig. 10(b)) and a double pulse (Fig. 10(c)) there exists an ambiguity in the FROG CRAB traces. This is the intermediate regime we studied in [1]. This ambiguity can be removed by stabilizing the CEP of the fundamental laser pulse. While the position of the burst(s) underneath the envelope cannot be determined without CEP stabilization, the attosecond pulse structure of the individual attosecond bursts, as well as the overall intensity envelope, can be retrieved [1].

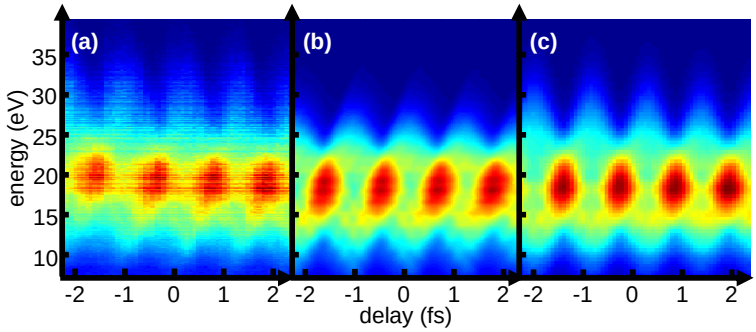

Fig. 11. Comparison of (a) experimental data, (b) GP algorithm, and (c) direct simulations of FROG CRAB traces using optimized EUV pulse parameters.

Lastly, we compare the reconstructed traces using the GP algorithm (Fig. 11 (b)) which does not contain the dependence on final photoelectron kinetic energy, with the progressive fitting

#105342 - $15.00 USD Received 15 Dec 2008; revised 1 Mar 2009; accepted 5 Mar 2009; published 9 Mar 2009

simulation code (Fig. 11 (c)) which contains the final photoelectron kinetic energy dependence. Visually it is obvious that the simulation code achieves a better agreement with the experimental trace Fig. 11 (a) than the GP algorithm with the $W \rightarrow W_0$ approximation. Also, in the simplified geometry (2° photoelectron detection angle and CEP stabilized) of [8] there is a systematic error between experimental and reconstructed trace due to this neglected energy dependency, which leads to ponderomotive shifts that are too weak at high photoelectron energies and too strong at low photoelectron energies. It was found [16] that this energy dependence is only negligible if the bandwidth of the attosecond pulse is small compared to the center energy, which is not fulfilled in [8] and the data presented here.

Thus it would be desirable that reconstruction algorithms such as the GP and PCGP [31] include the energy dependence in future implementations.

7. Interpretation of single attosecond pulse generation mechanism

In this section we give a qualitative explanation for the main experimental result of this paper, which demonstrates the generation of a single isolated attosecond pulse from a $\approx$ 15 fs, CEP unstabilized driving pulse. In essence, under our experimental conditions, efficient EUV generation is only possible on the leading edge of the driving pulse, before the coherence length gets too short due to the rapidly rising time-dependent ionization caused by the high-intensity driving pulse.

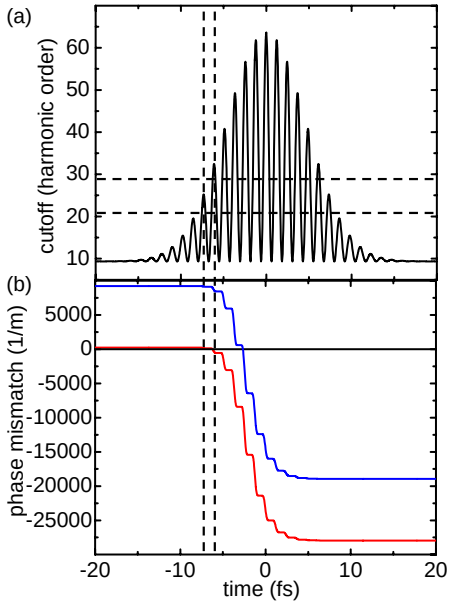

Fig. 12. (a) EUV cutoff harmonic as a function of time, determined from instantaneous intensity. (b) phase mismatch [14, 52] for the 25^{th} harmonic versus time for straight fiber (red), effect of employing a QPM fiber for same pulse parameters (blue). Horizontal dashed lines: region of experimentally generated EUV spectrum. Vertical dashed lines: guides to the eye highlighting the half-cycles in which efficient EUV generation is possible: Earlier, the instantaneous intensity is too low to generate the experimental spectrum (lower harmonics are absorbed in the generating Argon gas, and not reflected by EUV mirror). Later, large phase mismatch prevents coherent build-up of EUV radiation.

On the leading edge of a femtosecond pulse, every consecutive half-cycle has a higher in-

#105342 - $15.00 USD Received 15 Dec 2008; revised 1 Mar 2009; accepted 5 Mar 2009; published 9 Mar 2009

stantaneous intensity, so that in each half-cycle a new spectral range of EUV radiation with a higher cutoff than in the previous half-cycle can be generated, see Fig. 12 (a). This has been described in [32, 33, 23] and recently named "half-cycle cutoffs". If now from one half-cycle to the next, high harmonic generation can be suppressed, then the last half-cycle produces a spectral continuum corresponding to the bandwidth of radiation that was not accessed in the previous half-cycle. If lower-energy emission produced in more than one half-cycle is spectrally filtered out, a single isolated attosecond pulse remains.

In our case, a dynamic phase mismatch between driving laser and EUV radiation provides the mechanism that rapidly shuts off EUV generation. The phase mismatch is given by

$$\Delta k(t) = q \cdot k_{laser}(t) - k_q \tag{19}$$

where k_q is the wave vector of the q'th harmonic, and the fundamental laser wave vector $k_{laser}(t)$ is given by [14]

$$k_{laser}(t) \approx 2\pi/\lambda + \frac{2\pi N(1-\eta(t))\delta(\lambda)}{\lambda} - N\eta(t)r_e\lambda - \frac{u_{nm}^2\lambda}{4\pi a^2} \tag{20}$$

Here, N is the total gas density (neutral gas plus plasma), $\eta(t)$ is the time-dependent ionization fraction, $\delta(\lambda)$ describes the dispersive characteristics of the atom, r_e is the classical electron radius, a is the waveguide radius, and u_{nm} is the m^{th} root of the $(n-1)^{th}$ Bessel function of the first kind and depends on the transverse modes coupled into the waveguide. The EUV radiation is not significantly affected by any of the three dispersion contributions, and its wave vector k_q in Eq. 19 is only slightly modified from its vacuum value. In our low-pressure Argon, as shown in Fig. 12 (b), initially the phase mismatch is small, and EUV generation can occur. As soon as the intensity starts to increase rapidly on the leading edge of the pulse, it generates a very rapidly increasing plasma density. This growing plasma contribution sweeps the phase mismatch through zero and then to large negative values, such that high harmonic generation is suppressed for all later half-cycles.

The spectral filtering of lower harmonics (produced in several of the early half-cycles), required to isolate a single attosecond pulse, is achieved by the Mo/Si EUV mirror focusing the radiation into the detection gas jet. In addition, low harmonics are already strongly absorbed in the Argon gas.

To further support the dynamic phase-matching mechanism we performed propagation simulations for the driving laser with the purpose of finding the best pressure and laser peak intensity parameters for ensuring phase matching at a specific time window. The propagation equation we used is a one dimensional version of the extreme-nonlinear optics propagation equation developed by Geissler et al.[54] modified to include neutral gas dispersion and waveguide dispersion. The ionization of the medium was calculated using an ADK-based model[55]. As the generated high harmonics propagate with virtually no dispersion they can be considered to propagate at the speed of light. Because the propagation equation is calculated in a frame moving at the speed of light the degree of overlap of the laser pulse as it propagates in the medium with the one at the beginning of the medium is a measure for the temporal phase mismatch: at those times where there is perfect overlap the generation of the high harmonics would be completely phase matched. A similar approach was used to explain the generation of sub-optical cycle, CEP insensitive, EUV pulses [53]. To find the best parameters for our case we defined a phase-matching-criterion: the temporal overlap in the desired time-window divided by the temporal overlap outside this time window, integrated over the propagation coordinate, should be as large as possible. The time window was defined as the interval between the moment the laser intensity is high enough for generation of the 21^{st} harmonic to the moment it is high enough for the generation of the 29^{th} harmonic (as indicated in Fig. 12). Plots of this phase-matching-

#105342 - $15.00 USD Received 15 Dec 2008; revised 1 Mar 2009; accepted 5 Mar 2009; published 9 Mar 2009

criterion are shown in Fig. 13 a-b for two different values of CEP. Warmer colors correspond to better phase-matching-criterion. We note that the best pressure is almost the same for the two different CEP values while the best peak intensity changes by $\sim 10\%$ indicating only a small sensitivity to the CEP value. The estimated best peak intensity is different by only ten percent from the one estimated in the experiment while the estimated best pressure is about half of that estimated in the experiment which at such low pressures (~ 10 Torr) could be within the experimental estimation error. In Fig. 13 c-d the laser pulse at the end of the medium overlapped over the pulse at the beginning of the medium is shown for the two CEP cases for the best parameter values. As can be seen the overlap is optimized at the desired time window.

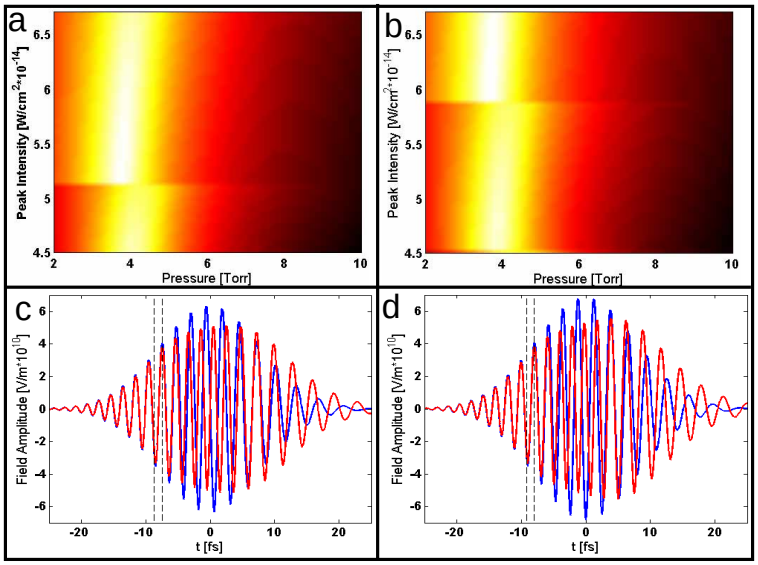

Fig. 13. Conditions for dynamic phase matching. Phase-matching-criterion for the time window in which the 21^{st}-29^{th} harmonics are first generated as a function of the laser peak intensity and gas pressure for (a) $CEP = \pi/2$ (b) $CEP = 0$. Warmer colors represent better phase matching. The corresponding temporal overlap of the laser pulse at the end of the medium (red) over the pulse at the beginning of the medium (blue) is shown in (c) and (d).

The numerical results of Fig. 13 indicate a blue-shift in the spectrum. This does not agree with measurements of the spectrum before and after the fiber, which showed only a small amount of reshaping. The reason for this discrepancy is that we used here one-dimensional simulations relevant only to the center of the radial laser intensity profile where the nonlinear conversion process is most efficient. Taking into account the radial intensity distribution combined with the low pressure within the fiber would wash out this blue-shift in a spectral measurement. For example, simulations we did indicate that once the field amplitude reduces to 60% of its peak value the spectral blue shift is only around 10% of the spectrum FWHM. In addition, the simulation assumed the same pressure conditions all along the fiber, while in the experiment a pressure gradient towards the end of the fiber could also reduce the spectral distortion. While the radial averaging reduces the spectral distortion, it does not destroy the dynamic phase-matching mechanism: the length scale needed for this mechanism is on the order of several coherence lengths (a few mm).

#105342 - $15.00 USD Received 15 Dec 2008; revised 1 Mar 2009; accepted 5 Mar 2009; published 9 Mar 2009

8. Outlook

In Ref. [1] we reported a technically simplified method for generating sub-optical cycle EUV radiation, consisting of either a single attosecond burst with a small pre-and post-pulse, or a double attosecond burst. The radiation was spectrally narrow and energy-tunable simply by changing pressure and intensity in the hollow waveguide, making it a very useful tool for future investigations of state-selective molecular and materials dynamics.

In the present study we reported the production of single isolated attosecond pulses in a straight hollow-core waveguide. This generation mechanism in this case is limited to the energy range we observed – as the pressure in the waveguide is increased, the quasicontinuous spectrum evolves towards separated harmonics. Adjustment of other parameters such as the pulse energy may make it possible to extend this study to the generation of attosecond pulses with tunable center wavelength. In addition, the use of different generation gases in the hollow-core waveguide and spectral filtering with EUV mirrors may allow for tuning. While the position of individual harmonics is only weakly CEP dependent in our regime, it remains to be studied if tunability of the spectral envelope (i.e. center energy) could be achieved in a hollow-core waveguide by changing the CEP of the driving pulse, as was shown for a 2 mm gas cell [23].

We believe that macroscopic effects [34, 46] are an important parameter for single attosecond pulse generation and can be used to generate tunable isolated attosecond pulses from multicycle driving laser pulses. One possible route to change the center wavelength of the attosecond pulse would be to employ quasi-phase-matching (QPM) methods [25]. In QPM one employs e.g. periodically modulated fibers to add a constant offset to the phase mismatch. This offset is tunable by changing the modulation period, and allows to shift the phase-matching window in time (see Fig. 12), and thereby one could phase-match half-cycles of different instantaneous intensities. This could create a short temporal window closer to the maximum intensity of the laser pulse and therefore could lead to the generation of a continuum at higher energies.

Alternatively, the use of spatiotemporal shaped driving pulses for isolated attosecond pulse generation could be investigated [45, 34]. This technique produces fundamental pulses with a fast rising edge, which should be well suited for generating isolated attosecond pulses.

Finally we note that the spatial mode profile of the driving laser in the hollow-core waveguide is a very important parameter in determining the spectral and temporal structure of the generated EUV radiation, and that therefore it is worth studying the separate contributions from the spatial mode profile and temporal profile of the fundamental pulse in detail [36].

9. Conclusion

In conclusion, we have shown experimentally that it is possible to generate a single isolated attosecond pulse with ≈ 15 fs driving pulses, by using dynamic phase-matching in a noble-gas filled hollow-core waveguide combined with spectral filtering. To temporally characterize the pulse, we have used photoelectron energy resolved two-color cross correlation and both a GP algorithm and direct simulations of the FROG CRAB traces. These were both extended from the conventional, angularly restricted photoelectron detection and CEP stabilized fundamental pulses, to a more efficient $2-\pi$ detection scheme and CEP unstabilized pulses. Both reconstruction methods agree very well on the temporal structure of the EUV pulse, finding a near-transform limited isolated EUV burst of ≈ 200 attoseconds FWHM.

Acknowledgments

We thank Farhad Salmassi, Andy Aquila, and Yanwei Liu for fabricating the EUV mirror. The authors gratefully acknowledge support from the National Science Foundation Physics Frontier Center and Engineering Research Center in EUV Science and Technology.

#105342 - $15.00 USD Received 15 Dec 2008; revised 1 Mar 2009; accepted 5 Mar 2009; published 9 Mar 2009